Needle Aligned Ultrasound Image-Guided Access Through Dual-Segment Array

Ashiqur Rahaman ⬤, Yichuan Tang ⬤, *Graduate Student Member, IEEE*,
Shang Gao ⬤, *Graduate Student Member, IEEE*, Xihan Ma ⬤, Igor Sorokin,
and Haichong K. Zhang ⬤, *Member, IEEE*

Abstract—Ultrasound (US) guided access for percutaneous nephrolithotomy (PCNL) is gaining popularity in the urology community as it reduces radiation risk. The most popular technique involves manual image-needle alignment. A misaligned needle however needs to be retracted and reinserted, resulting in a lengthened operation time and complications such as bleeding. These limitations can be mitigated through the co-registration between the US array and needle. The through-hole array concept provides the primary solution, including a hole at the center of the array. Because of the central opening, the image-needle alignment is achieved inherently. Previous literature has described applications that are limited to superficial and intravascular procedures, suggesting that developing a through-hole array for deeper target applications would be a new breakthrough. *Objective.* Here, we present a dual-segment array with a central opening. As the prototype development, two segments of 32-element arrays are combined with an open space of 10 mm in length in between them. *Method.* We conducted phantom and *ex-vivo* studies considering the target depth of the 80–100 mm range. The image quality and needle visibility are evaluated by comparing the signal-to-noise ratio (SNR), full width at half maximum (FWHM), and contrast-to-noise ratio (CNR) results measured with a no-hole linear array under equivalent conditions. An *ex-vivo* study is performed using porcine kidneys with ceramic balls embedded to evaluate the needle access accuracy. *Results and conclusion.* The mean needle access error of 20 trials is found to be 2.94±1.09 mm, suggesting its potential impact on realizing a simple and intuitive deep US image-guided access.

Ashiqur Rahaman is with the Department of Robotics Engineering and Department of Biomedical Engineering, Worcester Polytechnic Institute, USA.

Yichuan Tang, Shang Gao, and Xihan Ma are with the Department of Robotics Engineering, Worcester Polytechnic Institute, USA.

Igor Sorokin is with the Department of Urology, University of Massachusetts Medical School, USA.

Haichong K. Zhang is with the Department of Robotics Engineering, Department of Biomedical Engineering, and Department of Computer Science, Worcester Polytechnic Institute, Worcester, MA 01609 USA (e-mail: hzhang10@wpi.edu).

Index Terms—Needle-image alignment, Percutaneous intervention, Ultrasound-guided intervention, Dual-segment array.

I. INTRODUCTION

A. Clinical Background

PERCUTANEOUS nephrolithotomy (PCNL) is one of the gold standard treatment procedures for removing kidney stones, typically >1 cm in size [1], [2], [3], [4]. The procedural steps of this clinical treatment are as follows: 1) needle targeting of the desired calyx to access, 2) dilation and establishing a percutaneous tract, and 3) fragmentation and kidney stone extraction. These procedural steps are often performed under fluoroscopy guidance and ultrasound (US) guidance [1], [4].

The fluoroscopy-guided approach provides a clear projection view of the kidney, allowing accurate identification of the needle insertion position targeting the desired calyx to puncture [5]. Despite the strengths, fluoroscopy-guided access involves the risk of radiation exposure to patients and healthcare providers [6], [7]. Other concerns include missing key soft tissue landmarks such as pleura, spleen, and liver [8], [9], which are well visible in US images. Furthermore, the depth information for kidney puncture is often lacking, so the operator must rely on their sensation to navigate and advance the needle until it reaches the calyx [9].

On the other hand, the US-guided approach provides a real-time radiation-less imaging approach for monitoring the needle trajectory passing through the image, confirming the needle is on track to reach the target, which brings more accuracy to needle insertion [9]. Yet, this approach is highly manual, and image-needle alignment requires hand-eye coordination of the operator [10], [11], [12], [13], [14], [15], imposing a high cognitive burden to articulate the US probe and needle simultaneously. A misaligned needle needs to be retracted and reinserted, resulting in increased operation time and complications such as bleeding [16]. In addition to the manual image-needle alignment, this approach is essentially angled (e.g., around 45 degrees [12]) because the center of the image plane is occupied by the US probe (Fig. 1). The inserted angled needle remains invisible until it comes within the field of view (FoV) of the US array, as shown in Fig. 1, increasing the risk of puncturing important structures such as blood vessels [17]. Another risk factor of angled needle
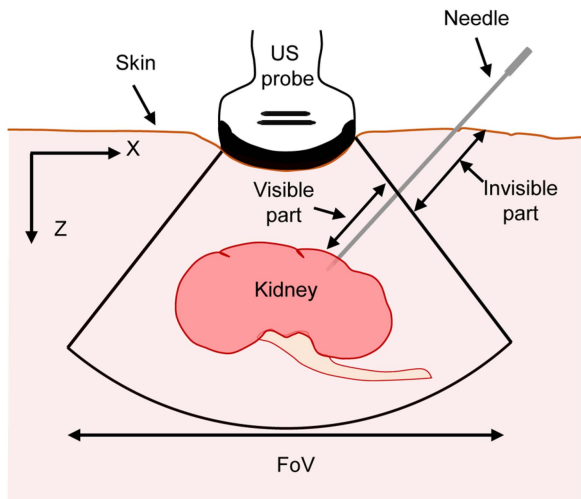
Fig. 1. Schematic of conventional US image-guided intervention approach showing the limitation of not visualizing the inserted needle from the beginning.

insertion is needle deflection [18]. Tsumura et al. [18] studied the rate of the needle deflection with respect to the needle insertion angle by considering the target is located at 100 mm in axial depth. The findings showed that 40 degrees angled needle has an almost 10 times higher needle deflection slope than what happens at 0-degree needle insertions [18]. Thus, the needle intervention accuracy of the current procedure solely depends on the hands-on experience of the operator.

B. Related Works

The challenges associated with skewed needle insertion could be mitigated by co-registering the US image and intervention tool [16]. Several efforts have been made to achieve co-registration, which are classified into two categories: external needle controller [19], [20], [21], [22], [23] and through-hole US array [24]. The external needle controller includes needle tracking [17], [23], mechanical needle guidance [25], and camera-assistance [26], [27] approaches, where the primary focus was given to tracking the invisible needle part, increasing computational as well as handling complexity [28].

The through-hole array, on the other hand, always keeps the needle path at the center of the image plane; as a result, it automatically co-registers with the needle. Kraochwil et al. [24] reported the first through-hole array in 1969, operating in amplitude (A)-mode for tracking the needle position. Inspired by Kraochwil's work, a few months later, the same group developed the brightness (B)-mode through-hole array, while the A-mode signal was kept used to detect the needle insertion motion [24]. Since then, the development of the through-hole array has been regularly reported in various modifications. Yet, the challenge in the through-hole array is the in-plane needle visualization, as the in-plane needle does not provide enough reflection for the B-mode imaging [13], [29]. For instance, Tanaka et al. [30], [31] included an additional circular aperture to visualize the inserted needle. Nonetheless, the dedicated needle visualization aperture helps the needle access but poses difficulties in releasing

the inserted needle. Recently, the same group demonstrated a high-frequency Through-hole linear array where they solved the previous limitations of needle manipulation by making a U-shaped slit, while the imaging depth was limited to 20 mm [32]. Gurun et al. [33], on the other hand, developed a miniaturized through-hole array operating in a capacitive sensing system dedicated to intra-vascular applications. The developed device's imaging depth was limited to 11 mm. Similarly, several groups have made an effort to develop a miniaturized through-hole array while limiting the axial depth to 10–15 mm [34]. In order to achieve deeper tissue diagnosis, Tsumura et al. [35], [36] developed a ring-array forward-viewing US array for efficient and intuitive needle insertion. The developed array includes 16 layers, where each layer comprises 32 elements, thus a total number of 512 elements. It was validated for a maximum axial depth of 100 mm, while in-plane needle visualization was not in the validation part [35], [36].

C. Contributions and Paper Organizations

The previously reported works on the through-hole array are limited to either the imaging depth or the feasibility study of the array, suggesting that developing a through-hole array for deeper application would be a new breakthrough. The deeper tissue diagnosis using a through-hole array will minimize complications and maximize procedural efficiency [16]. For instance, the through-hole array intuitively aligns the image and needle, providing a clear projection view of the inserted needle with respect to the target starting from the insertion. Thus, this approach will minimize the reinsertion rates and maximize the needle access performance.

We present a dual-segment array for efficient and intuitive needle access dedicated to large and deep target applications. The developed array comprises two segments, introducing a central opening for forward-viewing needle access. Several groups have reported the through-hole array configuration for needle puncture, which is similar to the proposed method [31], [37]. The main contribution is to introduce and study the applicability of the dual-segment array configuration for the deep target applications, such as PCNL. In addition to the image quality evaluation with variable conditions and parameters through simulation and phantom experiments, this is the first study evaluating needle insertion accuracy using the stone implanted *ex-vivo* porcine kidney, assessing the ability for the needle access guidance. The main contributions of this work are summarized as follows: (1) we introduce a dual-segment array for deep US image-guided needle access, and (2) the workflow development and experimental demonstration of through-hole US image-guided needle access using the *ex-vivo* porcine kidney.

The paper is organized as follows: Section II describes the materials and methods associated with the device design and image formation with the dual-segment array transducer. It includes theoretical background, experimental design, and description of the quantification parameters. Section III focuses on the results and discussion of the dual-segment array. The results are divided into three parts such as image quality evaluation, needle visibility evaluation, and needle access evaluation. Finally, Section IV
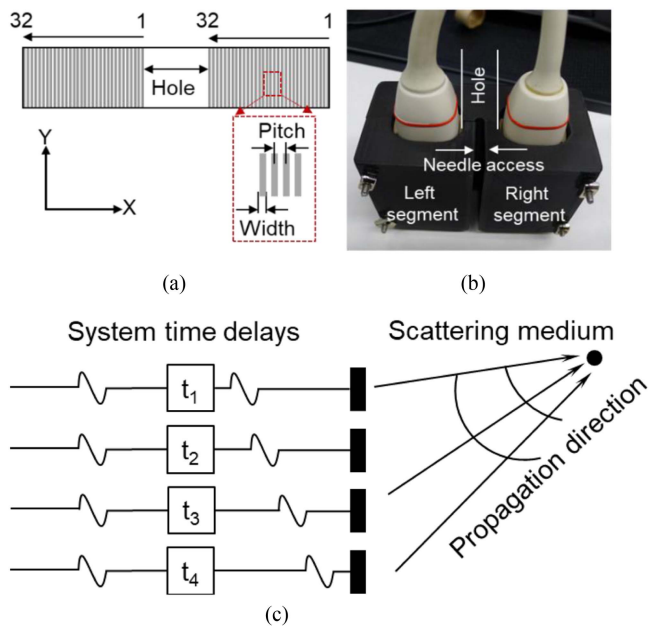
Fig. 2. Dual-segment array design and imaging sequence. (a) Schematic of the element distribution by introducing a center opening for needle insertion, (b) Assembled prototype in a custom-made probe housing, and (c) Focused beam steering of a segment.

discusses the accomplishments, shortcomings, and future directions.

II. MATERIALS AND METHODS

The development of the dual-segment array, along with the image formation, experimental setup, and image quality quantification metrics are presented in this section.

A. Prototype Development

Fig. 2(a) shows the schematic of the dual-segment US array. It includes 64 elements having a width of 0. 30 mm and a pitch of 0.32 mm. At the center of the developed US array, a hole of 10 mm in length is introduced by allocating 32 elements for each segment. Because of the center opening, the needle insertion path always stays at the center of the US image.

Unlike Ref. [31], the developed US array does not include any dedicated apertures for needle visualization; as a result, it enables an independent release mechanism for the inserted needle, as shown in Fig. 2(b). Instead of having a dedicated aperture, the beam steering approach is used to compensate for the image underneath the central opening. Although the 1-3 PZT-epoxy composites used in Ref. [32] are known better for noise response, the epoxy introduced thermal noise limits the transduction efficiency [38]. Thus, the developed array is expected to have better image quality at a higher depth.

B. Image Formation

Beam steering is a common and known method by which a US transmitter can transmit an acoustic beam at any angle (θ) in the lateral plane [39], [40], [41]. Fig. 2(c) shows an

arrangement where a small number of elements are considered for the simplicity of explanation. The elements are electronically excited in an angular lateral region of ± 80 degrees, enabling a visualization arc of 160 degrees.

The whole visualization arc comprises n number of ray beams with a beam width of $\Delta\theta$ and the transmission of each beam is electronically controlled by using delay time (Δt). The beam steering process ends at the last frame of the ray beam number. Thus, for a steering angle, $\Delta\theta$, the change of the angular position of the transmitted beams can be given as [41], $\Delta\theta = \theta/(n\text{-}1)$, where n is the number of ray being steered. On the other hand, the delay time (Δt) for each of the transmitted beam is given as [41], $\Delta t = n/c \times \tan(\theta)$, where c is the speed of sound, and θ is the whole visualization arc being visualized. In this work, an average speed of sound, i.e., 1540 m/s is used and the total number of rays is 256. The focal depth is set to 4 times of axial depth (110.88 mm).

Moreover, the beam steering is extended to be included focusing on the transmitted acoustic beam by controlling the delay time (Δt) to focus on any given angle in lateral region. Since the developed dual-segment US transducer has a center opening, the focused beams are steered at ± 80 degrees. Because at 80 degrees, the beam transmission happens at 47.13 mm far from the center of each segment, derived by R $\times \tan(\theta)$, where R is the radius of the visualization arc. During the transmit-receive cycles, one transducer was active and the other was in idle conditions at a frame rate 2.1 Hz.

$X(i,j)$ and $Y(i,j)$ are denoted as envelope detected data of two segments. Then, they are externally merged as follows,

$$D(i, j) = \sum_{k=1}^{n} X_k(i, j) \otimes Y_k(i, j) \tag{1}$$

where, $\otimes$, k, and $D(i,j)$ represent the translation and rotation between two data sets, the number of ray iterations, and the generated US image of the dual-segment array. Post-processing, such as log compression, is applied subsequently to compose a B-mode image.

C. Experimental Setup

Two sets of experimental setups are used in this work. One setup is for the dual-segment array, and another is for the ground truth with no hole. Because the efficacy justification of the developed array is performed using a no-hole linear array, which is denoted as "ground truth with no hole" throughout this paper.

For a dual-segment array, two commercially available phased-array US probes, i.e., P4-2 (Philips, Bothell, WA, USA) having a pitch of 0.32 mm and operating in 2.5 MHz center frequency, are used. The two probes are spatially positioned to form a total of 64 elements with an inter-distance of 10 mm, as shown in Fig. 2(b). The whole arrangement is placed in an in-house designed CAD model. The whole arrangement is connected to the data acquisition platform (Vintage 128, Verasonics, WA, USA) using a dual probe adapter (UTA 260-D, Verasonics, WA, USA), as shown in Fig. 3(a). In the data acquisition sequence program, an apodization of 32 elements is used for both probes to ensure a total number of 64 elements for the dual-segment array.
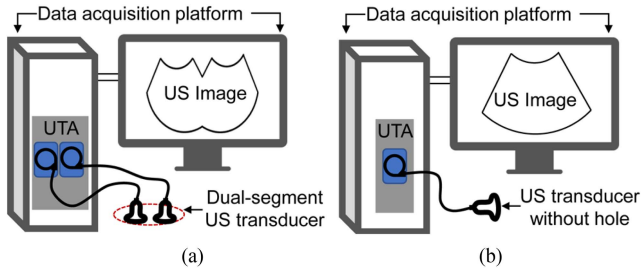
Fig. 3. Schematic of the experimental setup for, (a) Dual-segment array and (b) Ground truth with no hole.

Fig. 4. Simulated point targets US image of, (a) Left segment, (b) Right segment, (c) Dual-segment array, and (d) Ground truth with no hole.

The ground truth with no hole is a single P4-2 probe, where all 64 elements are activated without having any central opening for the 64-element ground truth with no hole. In this case, the US probe is directly connected to the data acquisition platform using a single probe adapter (UTA 260-S, Verasonics, WA, USA), as shown in Fig. 3(b).

In both cases, the arrays are operated at a 2.5 MHz center frequency and have an identical number of transmit rays in a range of ±80 degrees in the lateral axis.

D. Quantification Metrics

The acquired data are processed for image resolution and contrast evaluation by calculating SNR, FWHM, and CNR. The SNR is derived for both simulated and measured data by using the following equation [42],

$$\text{SNR} = 20 \times log_{10} \frac{|S_{\max}|}{\nu_{noise}} \quad (2)$$

where, $S_{\max}$ and ν_{noise} are the signal amplitude at the peak of subjected beam profile at each target and standard deviations of the background noise [42]. In addition to SNR, the FWHM is used to evaluate the image resolution. The FWHM is derived as follows,

$$\text{FWHM} = \frac{1}{r} \times (L_{\max} - L_{\min}) \quad (3)$$

where, $L_{\max}$-$L_{\min}$ presents the spectral width of the beam profile at the half magnitude that can be expressed as, $L_{\max}=L_{\min}=S_{\max}/2$. Also, r is the ratio. Moreover, the image distinguishability between the background and foreground of the generated US image is studied by using the CNR. The formula for deriving CNR is given as [20],

$$\text{CNR} = \frac{|\mu_1 - \mu_2|}{\sqrt{\phi_1^2 + \phi_2^2}} \quad (4)$$

where μ_1 and μ_2 are the mean pixel value of the selected region of interest (ROI), i.e., the foreground and background region. In addition, the standard deviation of corresponding pixel values is presented in ϕ_1 and ϕ_2, respectively.

III. RESULTS

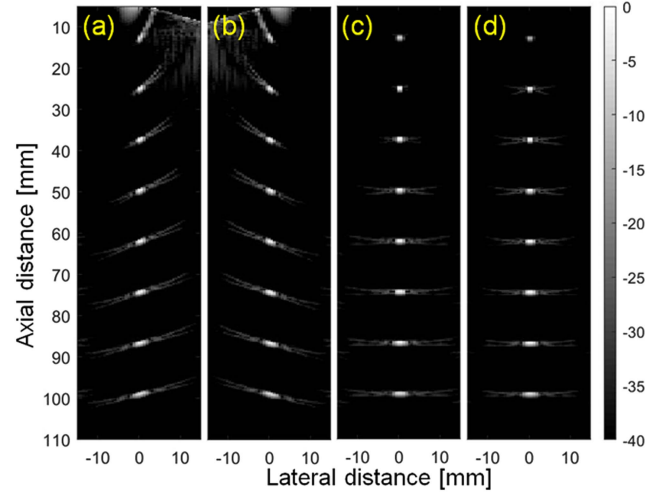Three steps evaluation is performed to validate the developed dual-segment array. Firstly, the image quality is evaluated using point and cyst targets phantoms. The evaluated image quality of the developed dual-segment array is justified by comparing the same image quantification metrics with ground truth with no hole measured under equivalent conditions. Secondly, the needle visibility is studied using a gelatin phantom and justified by comparing the same parameter of ground truth with no hole. Finally, the efficacy of the developed dual-segment array is evaluated for deep target needle access using ceramic balls embedded *ex-vivo* porcine kidney. This section presents all the evaluated results and their justifications.

A. Image Quality Evaluation

The point and cysts targets are considered to evaluate the image quality, where simulated and experimentally measured results are validated by comparing with the ground truth with no hole. The comparison is made in two ways: one segment and dual-segment array, and the dual-segment array and ground truth with no hole.

1) Point Spread Function: The simulation is performed using the Verasonics embedded media points. A total number of 8 media points are distributed in one vertical center line. The targets column contains a total number of 8 media points starting from 12.3 mm to 99 mm, an interval of 12.3 mm in depth. At first, each segment is simulated. The generated US images of the left segment and right segment (indicated in Fig. 2(b)) at a 40 dB dynamic range are shown in Fig. 4(a) and (b). Under equivalent conditions, Fig. 4(c) and (d) shows the generated US image of the dual-segment array and the ground truth with no hole, respectively.

The image quality evaluation of Fig. 4(a) and (d) is performed using the SNR and FWHM calculations derived by (2) and (3), respectively. The SNR results of one segment, dual-segment, and ground truth with no hole are compared, as shown in Fig. 5(a). The comparison shows that the SNR results of the one segment are lower than the dual-segment, which certifies that the echo intensity compounding both segments is working for
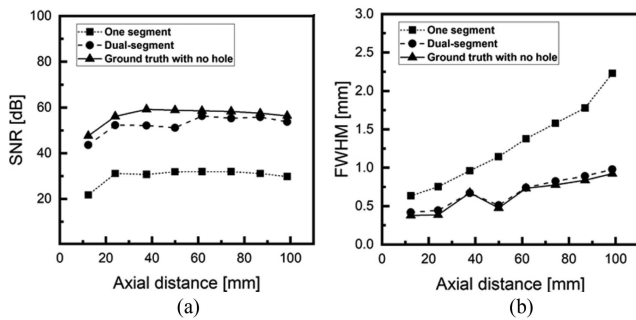
Fig. 5. Image quality evaluation results of simulated point targets (a) SNR, and (b) FWHM comparison among one segment, dual-segment and ground truth with no hole.

the dual-segment to attain higher SNR results. A similar effect can be found in the FWHM results, as shown in Fig. 5(b). The SNR and FWHM results of the dual-segment array are justified by comparing the same results of ground truth with no hole measured under equivalent conditions. The results comparison between the dual-segment array and the ground truth with no hole shows that the simulated results are compatible with each other, as shown in Fig. 5(a) and (b).

Nevertheless, the highest image resolution, i.e., a 0.63 mm of FWHM for one segment and a 0.41 mm FWHM for dual segments, is found at 12.3 mm, whereas they become 2.2 mm and 0.97 mm at 99 mm in axial depth. Similarly, the ground truth with no hole showed the highest resolution of 0.38 mm at 12.3 mm axial depth, and it becomes 0.92 mm at 99 mm depth. In both cases, the diameter of the media point is 0.1 mm; however, each of them could not achieve that diameter. It is obvious that the central opening was not the reason which can be confirmed by looking at the FWHM results of the ground truth with no hole. Therefore, it can be assumed that the pitch dimension could be the reason, meaning that the smaller pitch dimensions could improve the resolution.

Furthermore, the experimental demonstration of the image quality evaluation is performed using a commercially available US quality phantom (Model 040GS, CIRS, Virginia, USA). The vertical distance point targets up to 100 mm are used for the experimental demonstration. Thus, a total number of 5-point targets with an inter-distance of 20 mm are used. In addition to the vertical point targets, one horizontal point target is used in-between the 4th and 5th point targets from the top, as shown in Fig. 6(a) and (d). Each of the point targets is 0.1 mm in diameter. Similar to the simulation, each segment is used to scan the point targets first, and then the dual-segment array and ground truth with no hole are used.

Fig. 6(a) and (b) show the generated US image of the left segment and right segment. The merged US image by using (1) of the developed dual-segment array is shown in Fig. 6(c). After that, the ground truth with no hole is used to scan the point targets, as shown in Fig. 6(d). The image quality quantification is performed using (2) and (3), respectively for the SNR and FWHM. Fig. 7(a) and (b) shows the SNR and FWHM results comparison among each segment, dual-segment, and ground truth with no hole. Moreover, it should be noted that the
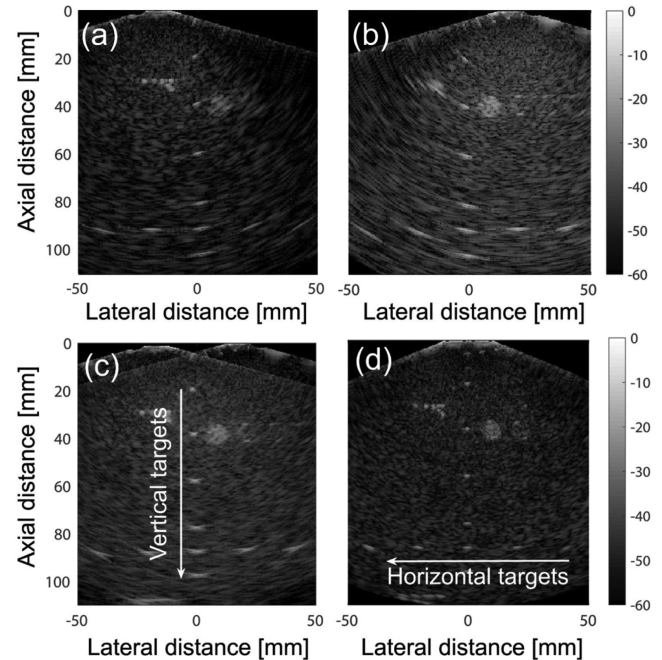

Fig. 6. Experimental results of point targets at -60 dB dynamic range. (a) Left segment, (b) Right segment, (c) Dual-segment array, and (d) Ground truth with no hole.
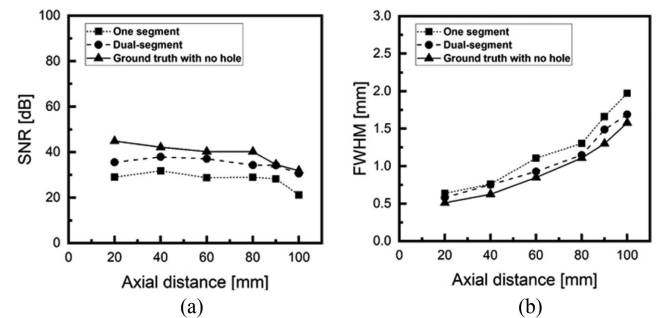

Fig. 7. Measured image quality evaluation results of point targets (a) SNR, and (b) FWHM comparison among one segment, dual-segment, and ground truth with no hole.

comparison is made using only one set of data from both segments since they are identical. The results are found compatible with each other, which experimentally certifies that the central opening does not affect the image quality significantly.

2) Cyst Phantom: The image quality assessment is extended toward the cyst phantom evaluation for image contrast justification. The cyst phantom simulation is performed using the Field II simulator [43], [44] by considering three anechoic cyst targets having a diameter of 6 mm. The cyst targets are placed at 50 mm, 70 mm, and 90 mm in axial depths. Fig. 8(a) and (b) shows the simulated US image of the left segment and right segment. The merged US image of the dual-segment array is shown in Fig. 8(c). After that, the ground truth with no hole is simulated, and the simulated US image is shown in Fig. 8(d).

Eq. (4) is used to calculate the CNR, and the results are presented in Table I. The one segment array showed an error between the measured cyst diameter and the actual cyst diameter
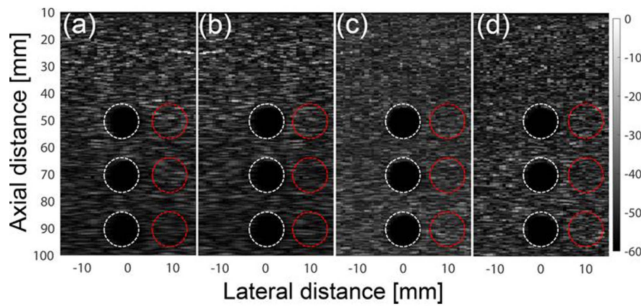
Fig. 8. Simulated US image at 60 dB dynamic range of cyst phantom for, (a) Left segment, (b) Right segment, (c) Dual-segment array, and (d) Ground truth with no hole. Dotted circle (white circle for anechoic region and red circle for background noise) represents ROI to estimate CNR.

TABLE I
IMAGE QUALITY EVALUATION OF SIMULATED 6-mm CYST TARGETS LOCATED AT 50, 70, AND 90 mm IN AXIAL DEPTH

Depth (mm)	Array	CNR ($\times 10^{-2}$)	Cyst Diameter	
			Measured (mm)	Error (%)
50	One segment	31.56	5.00	16.67
	Dual-segment	53.29	6.50	8.33
	Ground truth with no hole	57.87	6.50	8.33
70	One segment	27.45	4.50	25
	Dual-segment	41.79	6.50	8.33
	Ground truth with no hole	46.55	6.50	8.33
90	One segment	21.98	4.00	33.33
	Dual-segment	35.17	5.00	16.67
	Ground truth with no hole	38.22	5.50	8.33

(6 mm) of 33.33% at 90 mm in axial depth, whereas it is 16.67% for the dual-segment array. At the same depth, the ground truth showed an error of 8.33% by considering the measured and actual cyst diameter of 5.50 mm, and 6.00 mm, respectively. The errors of the dual-segment and ground truth with no hole are identical, which verifies the central opening does not affect the image contrast.

The experimental measurement of the cyst phantom is performed by using the commercially available US quality phantom (Model 040GS, CIRS, Virginia, USA), where three anechoic cysts targets are used. The image acquisition is performed until 100 mm, thus a total number of three embedded anechoic cyst targets at 40 mm, 70 mm, and 100 mm are scanned. The diameter of each cyst target is 8 mm. Fig. 9(a) and (b) show the generated US image of the left segment and right segments. The merged US image of the developed dual-segment array is shown in Fig. 9(c). After that, the ground truth with no hole is used to scan the cyst targets. The generated US image of ground truth with no hole is shown in Fig. 9(d). Similar to the simulated results, Eq. (4) is used to calculate the CNR, and the results are presented in Table II.

The CNR results of one segment, dual-segment, and ground truth with no hole at 100 mm in axial depth are found to be 18.58, 23.25, and 24.98, respectively. The dual-segment showed better contrast comparing the one segment due to the echo intensity compounding. Nevertheless, the ground truth with no hole showed higher CNR than dual-segment. Similarly, at 100 mm in axial depth, the errors between the measured and
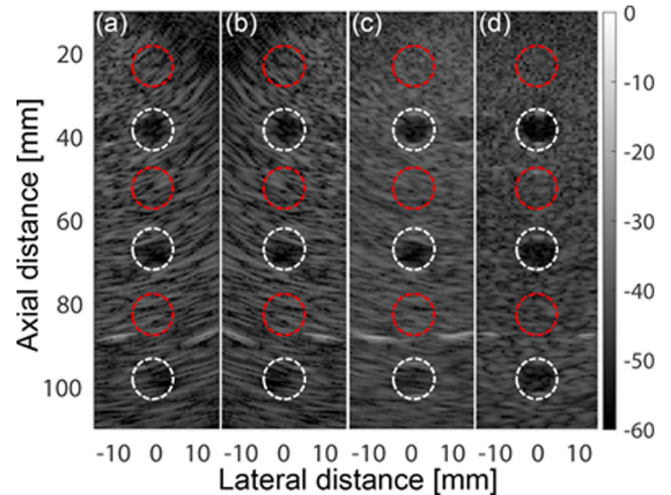

Fig. 9. Experimental measurement of cyst phantom at 60 dB dynamic range, (a), (b) Left and Right segment, (c) Dual-segment array, and (d) Ground truth with no hole. Dotted circle (white circle for anechoic region and red circle for background noise) represents ROI to estimate CNR.

TABLE II
IMAGE QUALITY EVALUATION OF EXPERIMENTALLY MEASURED 8-mm CYST TARGETS LOCATED AT 40, 70, AND 100 mm IN AXIAL DEPTH

Depth (mm)	Array	CNR ($\times 10^{-2}$)	Cyst Diameter	
			Measured (mm)	Error (%)
40	One segment	26.61	5.80	27.5
	Dual-segment	42.09	7.00	12.5
	Ground truth with no hole	42.12	7.50	6.5
70	One segment	20.59	4.50	43.8
	Dual-segment	31.39	6.00	25
	Ground truth with no hole	36.89	7.00	18.75
100	One segment	18.58	4.00	50
	Dual-segment	23.25	5.50	31.5
	Ground truth with no hole	24.98	6.00	25

actual cyst target diameter are found to be 43.8%, 50%, and 25%, respectively for one segment, dual-segment, and ground truth with no hole, where the dual-segment array showed an error of ~7% higher than ground truth with no hole, which could be the reason image scanning technique. For instance, the ground truth with no hole scans all the cysts by keeping them at the center, whereas for the dual-segment, each segment scans all the cyst targets by keeping them at the edge. The echo intensity reflected directly from the center improved the CNR of ground truth with no hole. Moreover, an error of ~7% should not be able to make a huge negative contribution, as we can see from the estimated cyst diameter. The measured cyst diameter of ground truth with no hole showed only 0.5 mm higher than that of dual-segment array. Therefore, it is noteworthy to mention that the center opening of the dual-segment array does not significantly damage the image quality comparing the ground truth with no hole.

B. Needle Visibility Evaluation

Needle visibility plays a vital role in US image-guided percutaneous interventions. Especially, the real-time feedback on the needle tip position allows physicians to determine where
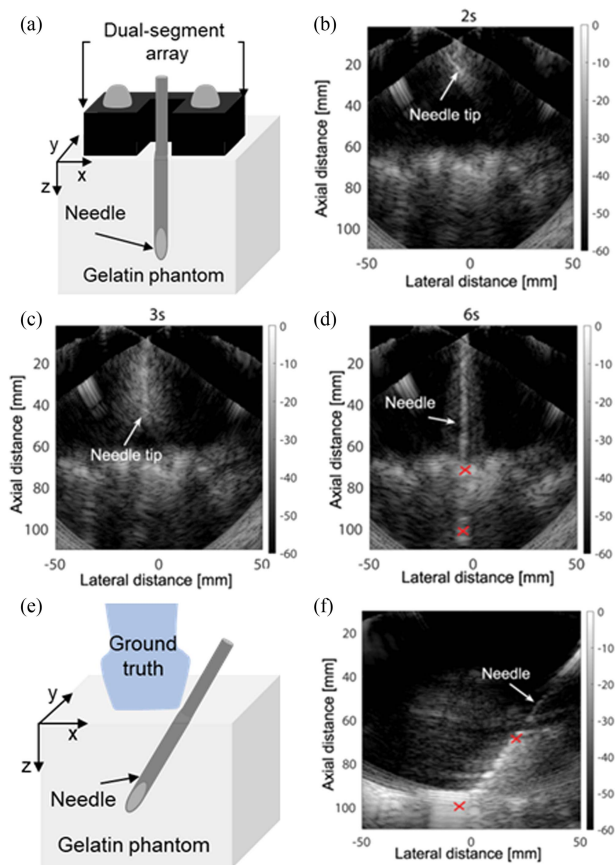
Fig. 10. Experimental demonstration of needle intervention at 60 dB dynamic range. (a) Schematic setup showing how the needle is inserted, (b)–(d) Generated temporal US images at 2 s, 3 s, and 6 s, respectively, (e) Schematic setup showing the conventional angled needle insertion, and (f) Generated US image of Fig. 10(e). Two red crosses (×) are marked at 70 mm and 100 mm in axial depth of Fig. 10(d) and (f) to justify the in-plane needle visibility.

TABLE III
NEEDLE VISIBILITY QUANTIFICATION AT 70 AND 100 mm IN AXIAL DEPTH

Depth (mm)	Dual-segment			Ground truth with no hole		
	SNR (dB)	FWHM (mm)	CNR ($\times 10^{-2}$)	SNR (dB)	FWHM (mm)	CNR ($\times 10^{-2}$)
70	40.59	1.93	39.92	54.79	1.62	52.37
100	38.45	2.81	13.32	38.65	2.59	11.50

Moreover, two red crosses are marked at 70 mm and 100 mm in axial depths in Fig. 10(d) to evaluate the needle visibility by comparing the conventional angled needle insertion approach. The angled needle insertion is performed using the schematic setup shown in Fig. 10(e). A protractor guides the needle insertion to keep the needle insertion path at 45 degrees, followed by Ref. [12]. The generated US image at a 60 dB dynamic range is shown in Fig. 10(f). The needle visibility is quantified by using SNR, FWHM, and CNR estimation for both approaches. The results are presented in Table III.

The SNR results of the developed dual-segment array at axial depths of 70 mm and 100 mm are found to be 40.59 dB and 38.45 dB, respectively. Whereas, at the same depths, the SNR results for the ground truth with no hole are found to be 54.79 dB and 38.65 dB, respectively. Both analyses use (2) for the SNR estimation. In addition to the SNR, the FWHM and CNR results of the dual-segment array at 100 mm axial depth are found to be 2.81 mm, and 13.32, respectively, using (3), (4). At the same depth, the ground truth with no hole showed an FWHM of 2.59 mm and CNR of 11.50. Thus, the results of the developed dual-segment array are compatible with ground truth with no hole, as presented in Table III. However, the higher SNR, FWHM, and CNR of the ground truth with no hole at 70 mm in depth are because of the angled needle insertion, which provides a higher amount of echo reflection. But the conventional angled needle insertion approach was unable to visualize the needle from the beginning of the insertion, as shown in Fig. 10(f), which was visible in a dual-segment array throughout the needle insertion, as shown in Fig. 10(b)–(d). The artifacts visible around the 70 mm depth could be due to multiple reflections from the container.

In actual clinical application, needle visibility starting from the needle insertion is more important because the inability of needle visualization often poses challenges in determining where the needle is with respect to the target. Even though the quantification parameters at 70 mm in depth are compromised, the developed approach maximizes the needle visualization from where it starts because of its intuitive image-needle alignment. It is, therefore, noteworthy to mention that the developed dual-segment will reduce the manual estimation of the needle path; rather, it will intuitively keep the needle path at the center of the US image.

In the next section, we will demonstrate the usefulness of the developed dual-segment array for needle access at an axial depth of ~80 mm.

C. Needle Access Evaluation

The image quality and the needle visibility results verify the uniqueness of the dual-segment array for intuitive needle

the needle tip is with respect to the target organ. Nevertheless, the conventional approach suffers from skewed needle insertion, relying on manual image-needle alignment. The developed through-hole array has a central opening, keeping the needle path always at the center of the generated US image, which enables intuitive image-needle alignment. Moreover, the challenge in in-plane needle insertion is its visualization because of less echo reflection.

The in-plane needle insertion and its visualization are evaluated by conducting an experiment. To do that, we used a gelatin phantom (G2500-type A, Sigma-Aldrich, St. Louis, MO, USA) without considering any targets. A general-purpose 18 G needle is used in this experiment. Fig. 10(a) shows the experimental setup for the needle visibility test. At first, the developed dual-segment array is used, and the generated US images with respect to the needle insertion time are shown in Fig. 10(b)–(d). **Movie file 1** demonstrates the real-time visibility of the needle intervention using a developed dual-segment array. The needle insertion presented in Fig. 10(b)–(d) indicates that the developed array clearly visualizes the inserted needle starting from the insertion because of the intuitive image-needle alignment.
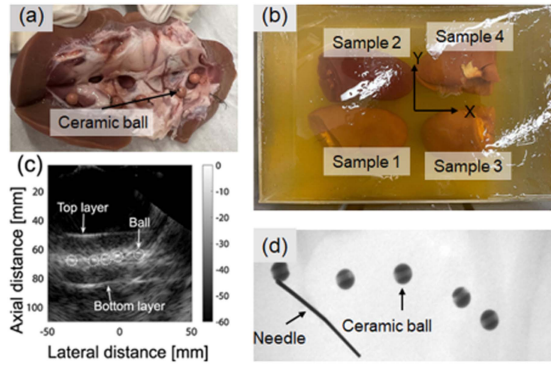
Fig. 11. Phantom preparation for the *ex-vivo* study, (a) Ceramic balls embedded in the porcine kidney, (b) Four kidneys are in a gelatin phantom for 20 trials of needle access, (c) the US, and (d) X-ray images of *Sample 1*.

insertion. One step further, deep US image-guided needle access is justified by targeting ceramic balls embedded in the *ex-vivo* porcine kidney.

In the *ex-vivo* study, four porcine kidneys are used. In each kidney, five ceramic balls are embedded as targets. The ceramic balls embedded in porcine kidneys are then placed in a gelatin phantom at an axial depth of ~80 mm. The number of kidneys, as well as the number of balls, are designed to perform 20 needle access trials. The *ex-vivo* procedural steps are as follows: 1) the target is identified using a real-time US image of the dual-segment array, 2) the through-hole needle is inserted guided by inherent image-needle alignment, and 3) the needle insertion accuracy is verified using a C-arm X-ray (Arcadis Orbic, Siemens, USA).

Fig. 11(a) shows one of the four *ex-vivo* pig kidneys embedded with 5 balls. The ceramic balls are embedded along the renal pelvis area to mimic the actual kidney stone's position. All the *ex-vivo* kidneys are placed in a single gelatin phantom to ensure their similar acoustic wave reflection as well as the image quality for needle access evaluation, as shown in Fig. 11(b). The four *ex-vivo* kidneys are denoted as *Samples 1-4*. Fig. 11(c) shows generated US image of *Sample 1* using a developed dual-segment array, where ceramic balls (as targets) can be found in dotted lines. Fig. 11(d) shows an X-ray image of the same targets in the *ex-vivo* porcine kidney.

Fig. 12(a)–(d) shows a complete set of needle access targeting the ceramic ball embedded in the *ex-vivo* porcine kidney. In the procedural steps at first, we scanned the targets using the developed dual-segment array. The generated US image is shown in Fig. 12(a), where the *ex-vivo* kidney structure and the embedded ceramic balls can be noticed. Right after selecting the target, the needle is inserted in the in-plane using forward-viewing. The needle tip and the target position are shown in Fig. 12(b). At this position, the needle spent 2 s to reach around ~25 mm in depth. After 3 s, the needle position is around ~40 mm with respect to the target position, as shown in Fig. 12(c). Finally, the needle tip is in close contact with the target, as shown in Fig. 12(d). The mean needle access time starting from the insertion is found to be 5±0.0041 s. In addition to the merely needle access time, the needle is visible throughout the insertion.
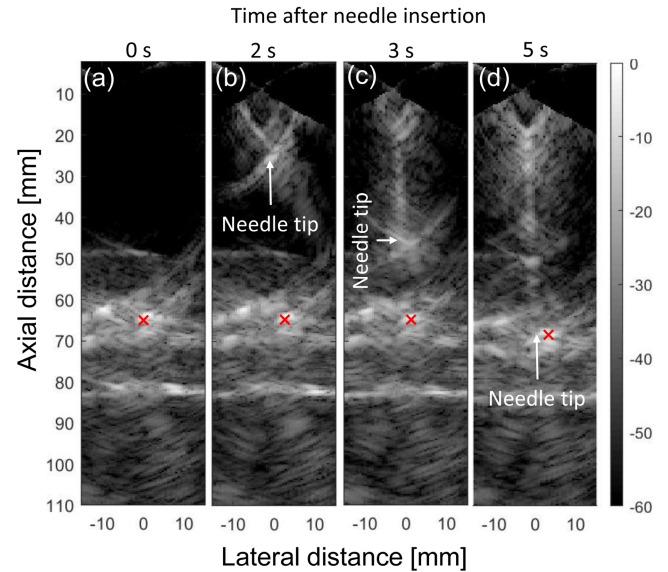

Fig. 12. US image-guided needle access using developed dual-segment array, (a) Target identification using US image, and (b)–(d) Temporal US images of the forward-viewing needle access. A red cross (×) in each image represents the target (ceramic ball) position.

Moreover, how accurately the needle is inserted towards the target is verified using the C-arm X-ray imaging technique, where each insertion is imaged twice, i.e., one image from the top view/X-Y plane and another image from the side view/X-Z plane. Thus, once the needle tip guided by a dual-segment US image reaches the target, the needle is released for an X-ray image.

The procedures (explained in Fig. 12) are repeated for 20 needle access trials, and a total of 40 X-ray images are taken. A summary of the X-ray images is presented in Fig. 13(a)–(i). For each plane, the accuracy is estimated by using the Euclidean distance between the needle tip and the target (ceramic ball). The details on the Euclidean distance estimation can be found in our previously reported work at Ref. [18]. Briefly, the diameter of the ceramic balls is measured and then averaged them. The average ceramic ball's diameter, i.e., 5.95 mm is used to calibrate the X-ray image in pixel/mm unit. Then, the distance between the needle tip and the center of the ceramic ball is converted into an mm unit. Finally, the radius of the ceramic ball is subtracted from the Euclidean distance by considering the needle at the surface of the ceramic balls. Based on the accuracy, all the needle access are categorized into three groups: satisfactory, good, and very good, respectively for >3 mm, <3 mm, and <1 mm needle insertion error, as shown in Fig. 13(a)–(i). The overall mean and standard deviation are 2.94±1.09 mm considering a 5.95 mm ceramic ball.

IV. DISCUSSION AND CONCLUSIONS

The primary intent of this work is to develop a through-hole US array, enabling an efficient and intuitive needle insertion mechanism for US image-guided percutaneous intervention. The through-hole array provides a central opening for needle access; as a result, the needle path always stays at the center
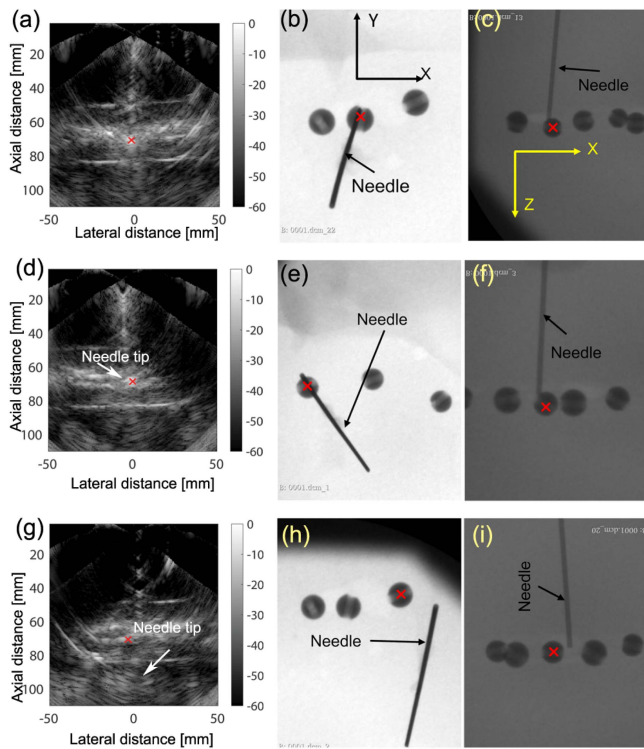
Fig. 13. Generated US images and X-ray images of dual-segment array-based needle access, (a)–(c) Very good, (d)–(f) Good, and (g)–(i) Satisfactory data sets in X-Y and X-Z planes. Red cross (×) symbols represent the target position.
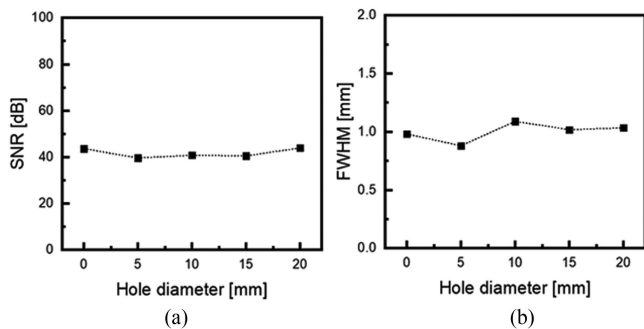

Fig. 14. The measured (a) SNR and (b) FWHM of a 100 mm depth point target by varying a central opening diameter.

of the generated US image. Due to its intuitive image-needle alignment, this approach mitigates the skewed needle insertion.

To get that aim, a novel US array, i.e., a dual-segment array was developed comprising a central opening and two segments. The effect of using a variable diameter of the central opening was evaluated through a Field II simulation, measuring the image quality of a deeply located point target [43], [44]. The dual-segment array was simulated with varying hole dimeters while maintaining the number of elements for each segment to be identical. A point target is fixed at center of the imaging plane at 100 mm in axial depth. The simulated results of SNR calculated by (2) and FWHM by (3), are compared with the ground truth with no hole (the result with 0 mm hole diameter), as presented in Fig. 14. The results indicate that there is minimal

image quality variation with the hole diameter changes when the number of elements is consistent. A 10 mm diameter is chosen for two reasons; first, the image quality is comparable with the ground truth with no hole, and second, a 10 mm diameter hole provides enough room for the clinician's workplace to insert and release the needle.

The development phase includes a thorough image quality analysis using point targets and cyst phantoms. Each of phantom evaluation was performed by considering SNR, FWHM, and CNR. Then, the needle visibility was performed down to the same quantification parameters. The image quality and needle visibility studies were justified by comparing a linear array having a similar number of elements with no hole. The primary consideration for the justification was to understand whether the image quality degrades due to the central opening of the developed array or not. The result comparisons between the dual-segment array and the ground truth with no hole showed that the quantification metrics, such as SNR, FWHM, and CNR were found compatible with each other, which indicates that the dual-segment array carries a similar level of image quality. Similar image quality was also achieved by conducting the experimental measurements. The needle visibility results showed that there was no remarkable difference between the developed dual-segment array and ground truth with no hole. Nevertheless, the watchable difference was found in needle insertion. For instance, the developed array was able to visualize the needle starting from the insertion, whereas the ground truth with no hole was unable. Therefore, it is noteworthy that the developed dual-segment array solves the skewed needle insertion by providing inherent image-needle alignment.

The developed dual-segment array was evaluated one step further through deep target US image-guided needle access. In this case, ceramic balls embedded ex-vivo porcine kidney were used, positing around 80 mm in axial depth. This experiment revealed that the developed dual-segment array provided real-time feedback on the needle position with respect to the target rather than relying on the manual image-needle adjustment. A total number of 20 needle access trials were made to estimate the needle access error. The needle access results were justified using a C-arm X-ray imaging technique.

The array developed in this work is significant for the actual clinical application. For instance, the mitigation of skewed needle insertion also minimizes skewed needle insertion-related complications. A major challenge of skewed needle insertion is that it depends on manual image-needle alignment, imposing a high cognitive load to keep the image-needle path well aligned with respect to the deep target. As a result, needle retraction and reinsertion are common practices that increase post-operative complications. The developed array has the potential to solve this problem because of its inherent image-needle alignment.

Despite significant contributions in image-needle-alignment, this work has some limitations. For instance, the developed array was made of commercially available two US probes, and thus we have limited control over the array dimensions. As for the FWHM results, the smaller pitch dimension could be helpful for better image quality. Secondly, further optimization of the imaging algorithm is required for better image quality. Finally,

this study is limited to the in-vitro and *ex-vivo* evaluations. For the efficacy justification, it is desired to perform an in-vivo study to observe how the developed array aligns the image and needle in live sensations such as breathing. Future work indicates the solution to these current limitations.

REFERENCES

[1] A. P. Ganpule et al., "Percutaneous nephrolithotomy (PCNL) a critical review," *Int. J. Surg.*, vol. 36, pp. 660–664, 2016.

[2] J. C. Dai et al., "Innovations in ultrasound technology in the management of kidney stones," *Urologic Clin.*, vol. 46, no. 2, pp. 273–285, 2019.

[3] D. T. Tzou et al., "Ultrasound use in urinary stones: Adapting old technology for a modern-day disease," *J. Endourol.*, vol. 31, no. S1, pp. S–89–S–94, 2017.

[4] D. Rodríguez and D. E. Sacco, "Minimally invasive surgical treatment for kidney stone disease," *Adv. Chronic Kidney Dis.*, vol. 22, no. 4, pp. 266–272, 2015.

[5] F. C. Ng et al., "Ultrasound-guided percutaneous nephrolithotomy: Advantages and limitations," *Invest. Clin. Urol.*, vol. 58, no. 5, pp. 346–352, 2017.

[6] B. Lojanapiwat, "The ideal puncture approach for PCNL: Fluoroscopy, ultrasound or endoscopy?," *Indian J. Urol.: J. Urological Soc. India*, vol. 29, no. 3, pp. 208–213, 2013.

[7] A. Sulieman and M. Alkhorayef, *Medical Imaging and Image-Guided Interventions*. London, U.K.: IntechOpen,, 2019.

[8] A. Malik et al., "Needle intervention system with mirror ultrasound imaging," Major Qualifying Project, Worcester Polytechnic Institute, MA, USA, 2020.

[9] Q. Liu et al., "Fluoroscopy versus ultrasound for image guidance during percutaneous nephrolithotomy: A systematic review and meta-analysis," *Urolithiasis*, vol. 45, no. 5, pp. 481–487, 2017.

[10] W. Brisbane, M. R. Bailey, and M. D. Sorensen, "An overview of kidney stone imaging techniques," *Nature Rev. Urol.*, vol. 13, no. 11, pp. 654–662, 2016.

[11] M. H. Lee et al., "Ultrasound guidance versus CT guidance for peripheral lung biopsy: Performance according to lesion size and pleural contact," *Amer. J. Roentgenol.*, vol. 210, no. 3, pp. W110–W117, 2018.

[12] G. Piton, G. Capellier, and H. Winiszewski, "Ultrasound-Guided Vessel Puncture: Calling for Pythagoras' help," *Critical Care*, vol. 22, pp. 1–2, 2018.

[13] R. K. Gupta et al., "Improving needle visualization by novice residents during an in-plane ultrasound nerve block simulation using an in-plane multiangle needle guide," *Pain Med.*, vol. 14, no. 10, pp. 1600–1607, 2013.

[14] A. D. Menhadji et al., "Technique for office-based, ultrasonography-guided percutaneous biopsy of renal cortical neoplasms using a novel transducer for facilitated ultrasound targeting," *BJU Int.*, vol. 117, no. 6, pp. 948–953, 2016.

[15] W. C. O'Neill, "Renal relevant radiology: Use of ultrasound in kidney disease and nephrology procedures," *Clin. J. Amer. Soc. Nephrol.*, vol. 9, no. 2, pp. 373–381, 2014.

[16] A. R. El-Nahas et al., "Post-percutaneous nephrolithotomy extensive hemorrhage: A study of risk factors," *J. Urol.*, vol. 177, no. 2, pp. 576–579, 2007.

[17] A. Mastmeyer, D. Fortmeier, and H. Handels, "Evaluation of direct haptic 4D volume rendering of partially segmented data for liver puncture simulation," *Sci. Rep.*, vol. 7, no. 1, pp. 1–15, 2017.

[18] R. Tsumura et al., "Preoperative needle insertion path planning for minimizing deflection in multilayered tissues," *IEEE Robot. Automat. Lett.*, vol. 3, no. 3, pp. 2129–2136, Jul. 018.

[19] Y. Tang et al., "Mirror-Integrated Ultrasound Image-Guided Access," *Proc. SPIE*, vol. 12034, pp. 484–490, 2022.

[20] Y. Tang et al., "Actuated reflector-based 3-D ultrasound imaging with synthetic aperture focusing," *IEEE Trans. Ultrason., Ferroelect., Freq. Control*, vol. 69, no. 8, pp. 2437–2446, Aug. 2022.

[21] C. K. Park et al., "A mechatronic guidance system for positron emission mammography and ultrasound-guided breast biopsy," *Proc. SPIE*, vol. 11315, pp. 342–349, 2020.

[22] J. Wu et al., "Robotic-assisted respiration-corrected 4D ultrasound imaging for image-guided interventions," in *Proc. IEEE 2nd Int. Conf. Multimedia Image Process.*, 2017, pp. 277–280.

[23] M. Arif, A. Moelker, and T. V. Walsum, "Automatic needle detection and real-time bi-planar needle visualization during 3D ultrasound scanning of the liver," *Med. Image Anal.*, vol. 53, pp. 104–110, 2019.

[24] H. Holm et al., "Ultrasound as a guide in percutaneous puncture technique," *Ultrasonics*, vol. 10, no. 2, pp. 83–86, 1972.

[25] P. M. Phal, D. M. Brooks, and R. Wolfe, "Sonographically guided biopsy of focal lesions: A comparison of freehand and probe-guided techniques using a phantom," *Amer. J. Roentgenol.*, vol. 184, no. 5, pp. 1652–1656, 2005.

[26] A. Benjamin et al., "Renal volume estimation using freehand ultrasound scans: An ex vivo demonstration," *Ultrasound Med. Biol.*, vol. 46, no. 7, pp. 1769–1782, 2020.

[27] K. Ito et al., "A probe-camera system for 3D ultrasound image reconstruction," in *Imaging for Patient-Customized Simulations and Systems for Point-of-Care Ultrasound*. Berlin, Germany: Springer, 2017, pp. 129–137.

[28] H. Scholten et al., "Improving needle tip identification during ultrasound-guided procedures in an aesthetic practice," *Anaesthesia*, vol. 72, no. 7, pp. 889–904, 2017.

[29] K. J. Chin et al., "Needle visualization in ultrasound-guided regional anesthesia: Challenges and solutions," *Regional Anesth. Pain Med.*, vol. 33, no. 6, pp. 532–544, 2008.

[30] Y. Tanaka et al., "Development and characterization of a small ring-shapedultrasonic probe for biopsies," *Japanese J. Appl. Phys.*, vol. 50, no. 7S, 2011, Art. no. 07HF03.

[31] Y. Tanaka et al., "Ultrasonic imaging of medical puncture using array probe," *Japanese J. Appl. Phys.*, vol. 53, no. 7S, 2014, Art. no. 07KF26.

[32] Y. Tanaka et al., "Needle tip detection using ultrasound probe for vertical punctures: A simulation and experimental study," *Diagnostics*, vol. 12, no. 2, 2022, Art. no. 527.

[33] G. Gurun et al., "Single-chip CMUT-on-CMOS front-end system for real-time volumetric IVUS and ICE imaging," *IEEE Trans. Ultrason., Ferroelect., Freq. Control*, vol. 61, no. 2, pp. 239–250, Feb. 2014.

[34] M. C. Finlay et al., "Through-needle all-optical ultrasound imaging in vivo: A preclinical swine study," *Light: Sci. Appl.*, vol. 6, no. 12, pp. e17103–e17103, 2017.

[35] R. Tsumura et al., "Ring-arrayed forward-viewing ultrasound imaging system: A feasibility study," *Proc. SPIE*, vol. 11319, pp. 111–118, 2020.

[36] R. Tsumura, S. Gao, Y. Tang, and H. K. Zhang, "Concentric-ring arrays for forward-viewing ultrasound imaging," *J. Med. Imag.*, vol. 9, no. 6, 2022, Art. no. 065002.

[37] S. Cochran et al., "P5C-5 design and validation of an ultrasound array optimised for epidural needle guidance," in *Proc. IEEE Ultrason. Symp.*, 2007, pp. 2255–2258.

[38] G.-S. Chen, H.-C. Liu, and Y.-L. Lin, "Comparison between 1-3 piezocomposite and PZT ceramic for high-intensity focused ultrasound transducer applications," in *Proc. AIP Conf.*, 2012, pp. 47–52.

[39] M. B. Rominger et al., "Ultrasound needle visibility in contrast mode imaging: An in vitro and ex vivo study," *Ultrasound Int. Open*, vol. 3, no. 02, pp. E82–E88, 2017.

[40] O. T. V. Ramm and S. W. Smith, "Beam steering with linear arrays," *IEEE Trans. Biomed. Eng.*, vol. BME-30, no. 8, pp. 438–452, Aug. 1983.

[41] K. Thomenius, "Instrumentation design for ultrasound imaging," *Biomedical Engineering And Design Handbook Vol. 2: Applications*, New York, NY, USA: McGraw-Hill, 2006, pp. 249–256.

[42] S. Gao et al., "Acoustic-resolution photoacoustic microscope based on compact and low-cost delta configuration actuator," *Ultrason.*, vol. 118, 2022, Art. no. 106549.

[43] J. A. Jensen, "Field: A program for simulating ultrasound systems," in *Proc. 10th Nordicbaltic Conf. Biomed. Imag.*, 1996, pp. 351–353.

[44] J. A. Jensen and N. B. Svendsen, "Calculation of pressure fields from arbitrarily shaped, apodized, and excited ultrasound transducers," *IEEE Trans. Ultrason., Ferroelect. Freq. Control*, vol. 39, no. 2, pp. 262–267, Mar. 1992.